SIAM J. SCI. COMPUT.
Vol. 35, No. 4, pp. B868–B889

A PARALLEL METHOD FOR SOLVING LAPLACE EQUATIONS WITH DIRICHLET DATA USING LOCAL BOUNDARY INTEGRAL EQUATIONS AND RANDOM WALKS*

CHANHAO YAN†, WEI CAI‡, AND XUAN ZENG†

Abstract. In this paper, a hybrid approach for solving the Laplace equation in general three-dimensional (3-D) domains is presented. The approach is based on a local method for the Dirichlet-to-Neumann (DtN) mapping of a Laplace equation by combining a deterministic (local) boundary integral equation (BIE) method and the probabilistic Feynman–Kac formula for solutions of elliptic partial differential equations. This hybridization produces a parallel algorithm where the bulk of the computation has no need for data communication between processors. Given Dirichlet data of the solution on a domain boundary, a local BIE is established over the boundary of a local region formed by a hemisphere superimposed on the domain boundary. By using a homogeneous Dirichlet Green's function for the whole sphere, the resulting BIE involves only the Dirichlet data (the solution value) over the surface of the hemisphere, while over the patch of the domain boundary intersected by the hemisphere, both Dirichlet and Neumann data are used. Then, first, the solution value on the surface of the hemisphere is computed by the Feynman–Kac formula, which is implemented by a Monte Carlo walk-on-spheres algorithm. Second, a boundary collocation method is employed to solve the integral equation on the aforementioned local patch of the domain boundary to yield the required Neumann data there. As a result, a local method of finding the DtN mapping is obtained, which can be used to find all Neumann data on the whole domain boundary in a parallel manner. Finally, the potential solution in the whole space can be computed by an integral representation using both the Dirichlet and Neumann data over the domain boundary.

Key words. Dirichlet-to-Neumann mapping, last-passage method, Monte Carlo method, walk on sphere, boundary integral equations, Laplace equation

AMS subject classifications. 65C05, 65N99, 78M25, 92C45

DOI. 10.1137/120875004

1. Introduction.

Fast and scalable parallel solvers for three-dimensional (3-D) Poisson and modified Helmholtz equations constitute a major computational cost for many large-scale scientific computing problems, such as Poisson/Helmholtz solvers in projection-type methods of incompressible flows [1], [2], and electrostatic potential problems in molecular biology, and in enforcing the divergence-free constraint of magnetic fields in magnetohydrodynamics (MHD) simulation of plasmas. In electrostatic capacitance problems of conductors, boundary element methods (BEMs) or finite element methods (FEMs) are often used by the engineering community to compute the charge density. Such methods include, for example, the indirect BEM FastCap

*Submitted to the journal's Computational Methods in Science and Engineering section April 25, 2012; accepted for publication (in revised form) June 5, 2013; published electronically August 13, 2013.

http://www.siam.org/journals/sisc/35-4/87500.html

†State Key Laboratory of ASIC & System, Fudan University, Shanghai, China (yanch@fudan.edu.cn, xzeng@fudan.edu.cn). The authors' work was supported partly by National Natural Science Foundation of China (NSFC) research projects 61125401, 61076033, 61228401, and 61274032, partly by the National Basic Research Program of China under the grant 2011CB309701, partly by the National Major Science and Technology Special Project 2011ZX 01035-001-001-003 of China during the 12th five-year plan period, partly by Shanghai Science and Technology Committee project 13XD1401100, and partly by the State Key Laboratory of ASIC & System Fudan University research project 11MS013.

‡Department of Mathematics & Statistics, University of North Carolina at Charlotte, Charlotte, NC 28223 (wcai@uncc.edu). This author's work was supported by the U.S. Army Research Office (grant W911NF-11-1-0364) and the NSF (grant DMS-1005441).

[3], [4], the direct QMM-BEM [5], the hierarchical HiCap and PhiCap [6], [7], and the parallel adaptive FEM ParAFEMCap [8]. BEMs [9] need to discretize the entire surface of a conductor, and sometimes even the dielectric interface, into small panels and construct a linear system by the method of moments or by collocation methods. On one hand, these deterministic methods are highly accurate and versatile, but on the other hand, they are global, namely, even if the charge density at only one point is required, a full linear system has to be constructed and solved. In general, the linear algebraic system resulting from a BEM is solved by an iterative method such as the multigrid method [10] or by the domain decomposition method [11], used either as a solver or as a preconditioner. Meanwhile, after the integral equation is discretized, the fast multipole method (FMM) [12] can be used in conjunction with a Krylov subspace iterative solver. All these solvers are $O(N)$ in principle, iterative in nature, and require expensive surface or volume meshes. The parallel scalability of these solvers on a large number of processors also poses many challenges and is the subject of current intensive research.

In contrast, random methods can give local solutions of partial differential equations (PDEs) [13], [14], [15], and they have been applied to obtain solutions at specific sites for many real-world problems such as the design of modern very-large-scale integration (VLSI) chips with millions of circuit elements in the chip-design industry. For instance, QuickCap [16], [17], the chip-design industry's gold standard as developed by the leading electronic design automation company Synopsys, is a random method. The key advantage of random methods is their localization. For example, QuickCap can calculate the potential or charge density at only one point locally without needing to find the solution elsewhere. Usually, random methods are based on the Feynman–Kac probabilistic formula, and the potential (or the charge density) is expressed as a weighted average of its values on the domain boundary [15]. The Feynman–Kac formula allows local solution of PDEs, and fast sampling techniques for diffusion paths using the walk-on-spheres (WOS) method are available for simple PDEs such as the Laplace or modified Helmholtz equation. However, it is impractical to use the probabilistic formula to find the solutions of these PDEs in the whole space because too much sampling is needed.

For current multicore petaflop computing platforms, the scalability of algorithms has become the major concern for the development of new numerical methods. Much research has been done in order to achieve such parallelism and scalability in the above deterministic algorithms for realistic engineering and scientific problems. To meet this challenge in this paper, we shall propose a hybrid method for computing the Neumann data (the normal derivative) of the solution from its Dirichlet data by combining the probabilistic Feynman–Kac formula with a deterministic local integral equation over patches of the domain boundary. The hybrid method allows us to get the Neumann data efficiently over local patches on the domain boundary, which results in a simple intrinsic parallel method for solving complete potential problems in general 3-D domains through an integral representation of the available Dirichlet and Neumann data.

The rest of the paper is organized as follows. In section 2, we present some background material on the Dirichlet-to-Neumann (DtN) mapping and the Feynman–Kac probabilistic solution of elliptic PDEs. In section 3, we first review the last-passage random-walk method proposed in [13] that can calculate the Neumann data (the charge distribution) *at one single point* on a flat surface on which constant Dirichlet data is assumed. Even though this is a very limited case of the DtN problem, it demonstrates some key issues and difficulties in how to use the Feynman–Kac

formula and the WOS scheme in finding the Neumann data. We then present a hybrid method that allows the calculation of Neumann data from general Dirichlet data on flat surfaces. In section 4, the hybrid method is extended to calculate Neumann data on *a patch* of a curved boundary with arbitrary Dirichlet data. Numerical tests are given in section 5 to show the accuracy and the potential of the proposed method. Conclusions, discussions for open research issues, and parallel aspects of the proposed method are given in section 6.

2. Background on the DtN mapping and solutions of potential equations. The DtN mapping between the Dirichlet data (the solution values) and the Neumann data (the normal derivatives of the solution) of a Poisson equation is relevant in both engineering applications and the mathematical study of elliptic PDEs. In electrostatic potential problems, the surface charge distribution σ_s on the surface $\partial\Omega$ of a conductor Ω, as required in the capacitance calculation of conductive interconnects in VLSI chips, is exactly the normal derivative of the electrostatic potential u as implied by Gauss's law for the electric field $\mathbf{E} = -\nabla u$. Namely, we have

$$\sigma_s = \mathbf{E}\cdot\mathbf{n}|_{\partial\Omega} = -\left.\frac{\partial u}{\partial \mathbf{n}}\right|_{\partial\Omega}. \tag{2.1}$$

On the other hand, the DtN mapping also plays an important role in the study of the Poisson equation. As the inhomogeneous right-hand side of a Poisson equation is usually known, we can use a simple subtraction technique to reduce the Poisson equation to a Laplace equation with modified boundary data. Therefore, in the rest of this paper we shall present our method for the Laplace equation on a domain Ω where general Dirichlet data are given on the boundary $\partial\Omega$. If we are able to compute the Neumann data from the given Dirichlet data, namely, the DtN mapping

$$\text{DtN:} \qquad u|_{\partial\Omega} \to \left.\frac{\partial u}{\partial \mathbf{n}}\right|_{\partial\Omega}, \tag{2.2}$$

then the solution $u(\mathbf{x})$ at any point $\mathbf{x}$ in the whole space can be found by simply using the integral representation

$$u(\mathbf{x}) = \int_{\partial\Omega} G(\mathbf{x},\mathbf{y})\frac{\partial u(\mathbf{y})}{\partial \mathbf{n_y}} ds_y - \int_{\partial\Omega} \frac{\partial G(\mathbf{x},\mathbf{y})}{\partial \mathbf{n_y}} u(\mathbf{y}) ds_y, \quad \mathbf{x}\in\Omega \text{ or } \Omega^c, \tag{2.3}$$

where $\mathbf{n_y}$ is the outward normal of the boundary of Ω or Ω^c to which $\mathbf{x}$ belongs and $G(\mathbf{x},\mathbf{y})$ is the fundamental solution of the Laplace operator, namely,

$$G(\mathbf{x},\mathbf{y}) = \frac{1}{4\pi}\frac{1}{|\mathbf{x}-\mathbf{y}|}. \tag{2.4}$$

A similar Neumann-to-Dirichlet (NtD) mapping from Neumann data to Dirichlet data can also be defined if the Neumann data results in a unique solution to the PDE. In either case, with both Dirichlet and Neumann data at hand, the solution of the Laplace equation can be obtained by the integral representation formula in (2.3).

Therefore, by finding the DtN or NtD mapping of the solution of the relevant elliptic PDE in an efficient manner, we can develop fast numerical methods for many applications in electrical engineering and fluid mechanics.

The Feynman–Kac formula [18], [19] relates the Ito diffusion path to the solution $u(\mathbf{x})$ of the following general elliptic problem:

$$L(u) \equiv \sum_{i=1}^{3} b_i(\mathbf{x}) \frac{\partial u}{\partial x_i} + \sum_{i,j=1}^{3} a_{ij}(\mathbf{x}) \frac{\partial^2 u}{\partial x_i \partial x_j} = f(\mathbf{x}), \quad \mathbf{x} \in \Omega,$$

$$u(\mathbf{x})|_{\mathbf{x}\in\partial\Omega} = \phi(\mathbf{x}), \tag{2.5}$$

where L is a uniformly elliptic differential operator, i.e., there exists a positive number $\mu > 0$ such that

$$\sum_{i,j=1}^{3} a_{ij}(\mathbf{x}) \xi_i \xi_j \geq \mu |\boldsymbol{\xi}|^2 \quad \text{if} \quad \mathbf{x} \in \Omega, \quad \boldsymbol{\xi} \in \mathbb{R}^3, \tag{2.6}$$

and $a_{ij}(\mathbf{x})$ and $b_i(\mathbf{x})$ are uniformly Lipschitz continuous on $\overline{\Omega} = \Omega \cup \partial\Omega$. Also the boundary $\partial\Omega$ of the domain Ω is assumed to be C^2 and the boundary data ϕ is assumed to be C^0, namely, $\phi \in C^0(\partial\Omega)$.

If $X_t(\omega)$ is an Ito diffusion defined by the stochastic differential equation

$$dX_t = b(X_t)dt + \alpha(X_t)dB_t, \tag{2.7}$$

where $B_t(\omega)$ is Brownian motion and $[a_{ij}] = \frac{1}{2}\alpha(x)\alpha^{\mathrm{T}}(x)$, then the following Feynman–Kac formula gives a probabilistic solution for (2.5):

$$u(\mathbf{x}) = E^x\left(\phi(X_{\tau_\Omega})\right) + E^x\left[\int_0^{\tau_\Omega} f(X_t)dt\right], \tag{2.8}$$

where the expectation is taken over all sampling paths $X_{t=0}(\omega) = \mathbf{x}$ and τ_Ω is the first hit time (or exit time) of the domain Ω. In this paper, we consider (2.8) only for the Laplace equation ($f \equiv 0$).

For the Laplace equation, the Ito diffusion is just Brownian motion. The solution of the Laplace equation can be simply rewritten in terms of a harmonic measure μ_Ω^x, which measures the probability of the Brownian paths hitting a given area on the boundary surface:

$$u(\mathbf{x}) = E^x(\phi(X_{\tau_\Omega})) = \int_{\partial\Omega} \phi(\mathbf{y}) d\mu_\Omega^x, \tag{2.9}$$

where

$$\mu_\Omega^x(F) = P^x\{\omega | X_{\tau_\Omega}(\omega) \in F, X_0(\omega) = \mathbf{x}\}, \ F \subset \partial\Omega, \quad \mathbf{x} \in \Omega. \tag{2.10}$$

The harmonic measure can be shown to be related to the Green's function $g(\mathbf{x}, \mathbf{y})$ of the Laplace equation in the domain Ω with a homogeneous boundary condition, i.e.,

$$\begin{aligned} -\Delta g(\mathbf{x}, \mathbf{y}) &= \delta(\mathbf{x} - \mathbf{y}), \quad \mathbf{x}, \mathbf{y} \in \Omega, \\ g(\mathbf{x}, \mathbf{y})|_{\mathbf{x}\in\partial\Omega} &= 0. \end{aligned} \tag{2.11}$$

By comparing (2.9) with the following integral representation of the solution of the Laplace equation in terms of the Green's function $g(\mathbf{x}, \mathbf{y})$,

$$u(\mathbf{x}) = -\int_{\partial\Omega} \phi(\mathbf{y}) \frac{\partial g(\mathbf{x}, \mathbf{y})}{\partial \mathbf{n}_\mathbf{y}} ds_y, \tag{2.12}$$

we can see that the hitting probability, now denoted as $p(\mathbf{x}, \mathbf{y})ds_y = \mu_\Omega^x([\mathbf{y}, \mathbf{y} + ds_y])$,

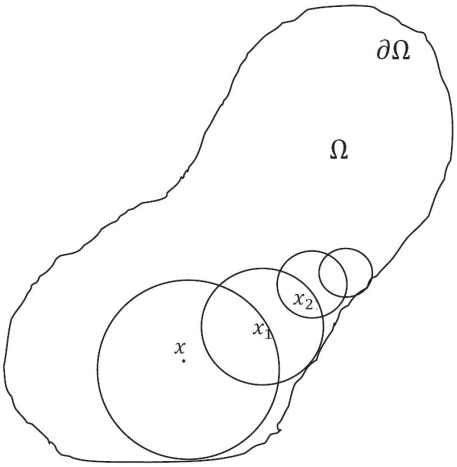

FIG. 2.1. *Illustration of WOS sampling of Brownian paths.*

has the following connection to the Green's function of the domain Ω [20]:

$$p(\mathbf{x}, \mathbf{y}) = -\frac{\partial g(\mathbf{x}, \mathbf{y})}{\partial \mathbf{n}_\mathbf{y}}. \tag{2.13}$$

Therefore, if the domain is a ball centered at the $\mathbf{x}$ where a path starts, we have a uniform probability for the path to hit the surface of the ball. This fact is a key factor in the design of random WOSs, which allows us to describe the Brownian motion and its exit location on $\partial\Omega$ without explicitly finding its trajectory. Instead, a sequence of walks or jumps over spheres allows the Brownian path to hit the boundary $\partial\Omega$ (for practical purposes, within an absorption ε-shell of $\partial\Omega$ as proposed in [21]). Specifically, as indicated by (2.13), the probability of a Brownian path hitting the surface of a sphere is given by the normal derivative of the Green's function for the sphere (with a homogeneous boundary condition). Therefore, if we draw a ball centered at the starting point $\mathbf{x}$ of a Brownian path, it will hit the surface of the ball with a uniform probability as long as the ball does not intersect with the domain boundary $\partial\Omega$. Thus we can make a jump for the Brownian particle to $\mathbf{x}_1$, sampled with a uniform distribution on the surface of the ball. Next, a second ball now centered at $\mathbf{x}_1$ is drawn, not intersecting with the domain boundary $\partial\Omega$, and the Brownian particle can make a second jump to $\mathbf{x}_2$ on the surface of the second ball. This procedure (as illustrated in Figure 2.1 and termed the WOS) [13], [22], [23] is repeated until the Brownian particle hits the domain boundary $\partial\Omega$ (within the absorption ε-shell of $\partial\Omega$) and the location of the hitting point is denoted as $\mathbf{x}_{\tau_\Omega}$. The value of the boundary data $\phi(\mathbf{x}_{\tau_\Omega})$ is then recorded, and eventually all such data are used to compute the expectation in (2.9). In real applications, due to the relation between the Green's function $g(\mathbf{x}, \mathbf{y})$ of a domain and the hitting probability, Green's function first passage (GFFP) methods for shapes other than spheres (such as rectangles) have been used in software including QuickCap to find capacitances of conductors in interconnect layouts, which are in general composed of rectangular shapes.

Moreover, in applying the Feynman–Kac formula (2.9) to find the potential in the infinite exterior domain (with a vanishing condition for the potential at infinity), since some paths go to infinity, truncation with a large sphere is used in our simulations of the WOS method in which trajectories outside the large sphere are ignored and

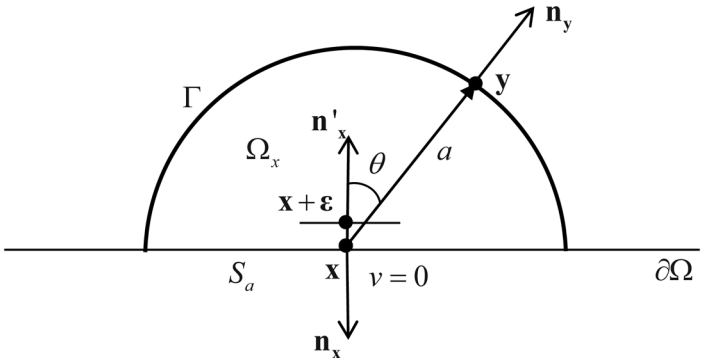

FIG. 3.1. *Illustration of the last-passage method for finding the Neumann data at a point* $\mathbf{x}$.

considered as ending at infinity where the potential vanishes. Theoretical estimates on the size of the truncation sphere can be found in [24].

3. Finding the Neumann data at one point on a flat boundary.

3.1. Last-passage algorithm for the charge density. In this subsection, we review the last-passage Monte Carlo algorithm proposed in [13] for the charge density, namely, the Neumann data, at one point on a flat *conducting* surface.

For a flat patch of the boundary $\partial\Omega$ of the domain $\Omega = \{z < 0\}$ in 3-D space where a constant Dirichlet boundary condition $u \equiv 1$ is assumed, we would like to compute the charge density at a point $\mathbf{x} \in \partial\Omega$, namely, the normal derivative of the exterior potential $u(\mathbf{x})$ outside Ω. In the last-passage method, a hemisphere of radius a is constructed and centered at $\mathbf{x}$ as shown in Figure 3.1. The hemispherical surface is denoted by Γ and the two-dimensional (2-D) disk of radius a centered at $\mathbf{x}$, namely, the intersection of the hemisphere and the conducting boundary $\partial\Omega$, is denoted by

$$S_a \equiv S_a(\mathbf{x}). \tag{3.1}$$

In the last-passage method [13], for the electrostatic potential $u(\mathbf{x})$, the quantity $v(\mathbf{x}) \equiv 1 - u(\mathbf{x})$ is considered instead, which satisfies

$$v(\mathbf{x}) = 0, \quad \mathbf{x} \in S_a, \tag{3.2}$$

and $v = 1$ at infinity (or on an infinitely large sphere). By viewing $v(\mathbf{x}+\varepsilon)$ as the probability of the Brownian particle at $\mathbf{x}+\varepsilon$ near the conducting surface $\partial\Omega$ diffusing to infinity *without ever coming back* to the conducting surface, it was shown in [13] that the following probabilistic expression for $v(\mathbf{x}+\varepsilon)$ holds:

$$v(\mathbf{x}+\varepsilon) \equiv 1 - u(\mathbf{x}+\varepsilon) = \int_\Gamma \widehat{g}(\mathbf{x}+\varepsilon, \mathbf{y}) p_{y\infty} ds_y, \tag{3.3}$$

where $p_{y\infty}$ is the probability of the Brownian particle at $\mathbf{y}$ diffusing to infinity without ever coming back to the conducting surface; thus $p_{y\infty} = 0$ if $\mathbf{y} \in S_a$, which is also the reason that the integral over S_a does not appear in (3.3). Moreover, the integral over Γ expresses the Markov property of the diffusing particle from $\mathbf{x}+\varepsilon$ to infinity with an intermediate stop on Γ. Specifically, $\widehat{g}(\mathbf{x}+\varepsilon, \mathbf{y})$ is the probability of the Brownian particle at $\mathbf{x}+\varepsilon$ hitting the boundary Γ, which has been shown to be given by (2.13)

via a homogeneous Green's function for the hemisphere over S_a, namely,

$$\widehat{g}(\mathbf{x}+\varepsilon,\mathbf{y}) = -\frac{\partial g}{\partial \mathbf{n}_y}(\mathbf{x}+\varepsilon,\mathbf{y}), \tag{3.4}$$

where $g(\mathbf{x},\mathbf{y})$ is defined in (2.11) for the hemisphere with homogeneous boundary conditions on both Γ and S_a. The analytical form of g can be obtained by the method of images with respect first to the spherical surface and then to the plane $z=0$, resulting in three images. More specifically, we have

$$g(\mathbf{x},\mathbf{x}_{\rm s}) = \frac{1}{4\pi}\frac{1}{|\mathbf{x}-\mathbf{x}_{\rm s}|} + \frac{1}{4\pi}\frac{q_{\rm k}}{|\mathbf{x}-\mathbf{x}_{\rm k}|} + \frac{1}{4\pi}\frac{q_{\overline{\rm s}}}{|\mathbf{x}-\mathbf{x}_{\overline{\rm s}}|} + \frac{1}{4\pi}\frac{q_{\overline{\rm k}}}{|\mathbf{x}-\mathbf{x}_{\overline{\rm k}}|}, \tag{3.5}$$

where in spherical coordinates the source location is $\mathbf{x}_{\rm s} = (\rho_{\rm s},\theta_{\rm s},\phi_{\rm s})$, the location of the Kelvin image with respect to the sphere is $\mathbf{x}_{\rm k} = (a^2/\rho_{\rm s},\theta_{\rm s},\phi_{\rm s})$, and the locations of their mirror images with respect to the plane $z=0$ are $\mathbf{x}_{\overline{\rm s}} = (\rho_{\rm s},\pi-\theta_{\rm s},\phi_{\rm s})$ and $\mathbf{x}_{\overline{\rm k}} = (a^2/\rho_{\rm s},\pi-\theta_{\rm s},\phi_{\rm s})$, respectively. Meanwhile, the corresponding charge magnitudes are $q_{\rm k} = -a/\rho_{\rm s}$, $q_{\overline{\rm s}} = -1$, and $q_{\overline{\rm k}} = a/\rho_{\rm s}$, respectively.

Now, to get the charge distribution σ_s, we use the relation in (2.1), i.e.,

$$\sigma_s = -\lim_{\varepsilon\to 0}\mathbf{n}_{x+\varepsilon}\cdot\mathbf{E}(\mathbf{x}+\varepsilon) = \lim_{\varepsilon\to 0}\frac{\partial u(\mathbf{x}+\varepsilon)}{\partial \mathbf{n}_x} = \frac{\partial u(\mathbf{x})}{\partial \mathbf{n}_x}. \tag{3.6}$$

By differentiating (3.3) along the $\mathbf{n}_x$ direction, we have

$$\frac{\partial u(\mathbf{x})}{\partial \mathbf{n}_x} = \int_\Gamma h(\mathbf{x},\mathbf{y}) p_{y\infty} ds_y \equiv \Sigma_{\rm LP}, \tag{3.7}$$

where $\Sigma_{\rm LP}$ is introduced as a shorthand for the integral over Γ for latter use, and

$$h(\mathbf{x},\mathbf{y}) = \frac{\partial^2}{\partial \mathbf{n}_x \partial \mathbf{n}_y} g(\mathbf{x},\mathbf{y}). \tag{3.8}$$

Here, for the hemisphere the weight function $h(\mathbf{x},\mathbf{y})$ can be computed analytically as

$$h(\mathbf{x},\mathbf{y}) = \frac{3}{2\pi}\frac{\cos\theta}{a^3}, \tag{3.9}$$

where θ is the angle between the two normal vectors $\mathbf{n}'_x$ and $\mathbf{n}_y$ as shown in Figure 3.1.

Next, we only need to compute $p_{y\infty}$ for $\mathbf{y}\in\Gamma$, namely, the probability of the Brownian particle at a point $\mathbf{y}\in\Gamma$ diffusing to infinity without ever returning to the conducting surface $\partial\Omega$. Due to the homogeneity of Brownian motion in the exterior domain $\Omega^c = \{z>0\}$, the WOS method introduced in section 2 can be used to calculate this probability. The integral over Γ in (3.7) can be approximated by Gauss quadrature because both $h(\mathbf{x},\mathbf{y})$ and $p_{y\infty}$ can be considered as smooth functions of $\mathbf{y}\in\Gamma$. Nonetheless, in [13], the integral $\Sigma_{\rm LP}$ is computed by first distributing N particles at locations over Γ based on a distribution density derived from (3.9) and then starting a Brownian diffusion path from each of those locations. Let $N_{\rm inf}$ be the total number of paths that take the particles to infinity. (In practice, it is when the particles hit a large sphere.) Then the following estimate is used:

$$\Sigma_{\rm LP} \simeq \frac{3}{2a}\frac{N_{\rm inf}}{N}. \tag{3.10}$$

The key equation in the last-passage algorithm is (3.7), which is based on (3.3) and the fact that $v(\mathbf{x})\equiv 0$ for $\mathbf{x}\in S_a$ on the conducting surface as indicated in (3.2). Therefore, for a general nonconstant Dirichlet boundary condition, the last-passage method is not applicable. In reality, the charge density at $\mathbf{x}$ will be influenced by the potential on the whole domain boundary.

3.2. Boundary Integral Equation-WOS method: Combining a Boundary Integral Equation and the Monte Carlo WOS method. For the last-passage method discussed above, the algorithm (3.7) is obtained using the isomorphism between the electrostatic potential and the diffusion problem. The limitation of the last-passage method is that it is applicable only in the case of constant Dirichlet data and flat boundaries. In this subsection, we adopt a different approach based on a boundary integral equation (BIE) representation of the charge density (the Neumann data) on the surface at a given point using the potential over a small hemisphere; the latter is to be computed by the random WOS method. As a result, this new method, a hybrid between deterministic and random approaches, is able to handle general variable Dirichlet boundary data and can also be extended to handle curved boundaries, as discussed in section 4.

Let us denote by Ω_x the domain formed by the hemisphere of radius a centered at $\mathbf{x}$ over the flat boundary S_a as in Figure 3.1. By applying the integral representation (2.3) of the solution of the Laplace equation with Green's function $g(\mathbf{x}, \mathbf{y})$ defined in (3.5) for the domain Ω_x and using the zero boundary value of $g(\mathbf{x}, \mathbf{y})$, we have

$$u(\mathbf{x}') = -\int_{\Gamma \cup S_a} \frac{\partial g(\mathbf{x}', \mathbf{y})}{\partial \mathbf{n_y}} u(\mathbf{y}) ds, \quad \mathbf{x}' \in \Omega_x. \tag{3.11}$$

In order to obtain the normal derivative of u at $\mathbf{x}$, we simply take the derivative with respect to $\mathbf{x}'$ along the direction $\mathbf{n_x}$ as $\mathbf{x}'$ approaches $\mathbf{x}$, and we obtain the following representation involving a hyper-singular kernel:

$$\frac{\partial}{\partial \mathbf{n_x}} u(\mathbf{x}) = -\lim_{\mathbf{x}' \to \mathbf{x}} \int_{\Gamma \cup S_a} \frac{\partial^2 g(\mathbf{x}', \mathbf{y})}{\partial \mathbf{n_x} \partial \mathbf{n_y}} u(\mathbf{y}) ds, \quad \mathbf{x} \in S_a. \tag{3.12}$$

Therefore, the integral expression for $\frac{\partial}{\partial \mathbf{n_x}} u(\mathbf{x})$ involves two integrals, one regular integral over the hemispherical surface Γ denoted by

$$\Sigma_1 = -\int_{\Gamma} \frac{\partial^2 g(\mathbf{x}, \mathbf{y})}{\partial \mathbf{n_x} \partial \mathbf{n_y}} u(\mathbf{y}) ds_y = -\int_{\Gamma} \left(\frac{3}{2\pi} \frac{\cos\theta}{a^3} \right) u(\mathbf{y}) ds_y, \tag{3.13}$$

where (3.9) has been used to get the second equality, and one hyper-singular integral over the disk S_a denoted by

$$\Sigma_2 = -\lim_{\mathbf{x}' \to \mathbf{x}} \int_{S_a} \frac{\partial^2 g(\mathbf{x}', \mathbf{y})}{\partial \mathbf{n_x} \partial \mathbf{n_y}} u(\mathbf{y}) ds_y, \tag{3.14}$$

and so we have

$$\frac{\partial}{\partial \mathbf{n_x}} u(\mathbf{x}) = \Sigma_1 + \Sigma_2. \tag{3.15}$$

Equation (3.15) is the starting point for the proposed hybrid method for a flat boundary. In computing the regular integral Σ_1, say, by Gauss quadrature over the hemispherical surface Γ, we need the solution $u(\mathbf{y})$ for $\mathbf{y} \in \Gamma$, and this solution can be readily computed by the Feynman–Kac formula (2.9) with the WOS sampling technique for Brownian paths. On the other hand, the singular integral Σ_2, with appropriate treatment of the hyper-singularity to be described in detail in the numerical test section, can be calculated directly with the given Dirichlet boundary data $u(\mathbf{y})$ for $\mathbf{y} \in S_a$. Therefore, the algorithm based on (3.15) involves the hybridization of

the random WOS method and a deterministic BIE method, and is thus termed the *BIE-WOS method*.

Remark. In comparing the last-passage method (3.7) with the BIE-WOS method (3.15), the former uses the relation between the Brownian motion of diffusive particles and the electric potential on a conducting surface to arrive at an expression for the surface charge density, namely, (3.7). On the other hand, the BIE-WOS method uses a hyper-singular BIE to get the similar expression (3.15), which has an additional contribution from the variable potential on the charged surface (the integral term Σ_2). Both methods use the WOS technique for particles starting on Γ, but at different locations. The last-passage method proposed in [13] initiates particles' walks starting from positions all over the hemisphere sampled using the probability given by (3.9), while the BIE-WOS method initiates the walks starting from selected Gauss quadrature points (up to 30×30 points in our test problems). Numerical results in section 5 show that for problems suitable for both methods, the two methods are comparable in the total number of walk paths as well as in accuracy and computational cost. (Refer to Test 4 in section 5.1.3.)

4. Finding Neumann data over a patch on a general boundary. In this section, we extend the BIE-WOS method to the case of general Dirichlet boundary data on curved domain boundaries. To achieve this goal, we superimpose a hemisphere over any selected portion of the domain boundary $\partial\Omega$; see Figure 4.1. The intersection of the domain boundary and the hemisphere is denoted by S and the surface of the hemisphere outside the domain Ω is denoted by Γ. The region bounded by S and Γ is denoted by Ω_S. Now let $G(\mathbf{x}, \mathbf{y})$ be the Green's function of the corresponding *whole sphere* with a homogeneous boundary condition, which can be easily obtained by just using the Kelvin image as discussed before. Then the integral representation (2.3) can be applied to the boundary of the domain Ω_S to yield the following identity:

$$
\begin{aligned}
u(\mathbf{x}) = &- \int_\Gamma \frac{\partial G(\mathbf{x}, \mathbf{y})}{\partial \mathbf{n_y}} u(\mathbf{y}) ds_y \\
&+ \int_S \left[-\frac{\partial G(\mathbf{x}, \mathbf{y})}{\partial \mathbf{n_y}} u(\mathbf{y}) + G(\mathbf{x}, \mathbf{y}) \frac{\partial u(\mathbf{y})}{\partial \mathbf{n_y}} \right] ds_y, \quad \mathbf{x} \in \Omega_S.
\end{aligned} \tag{4.1}
$$

It should be noted that the integral over Γ involves only the normal derivative of the Green's function since G vanishes on Γ by construction, and as a result, on Γ only the

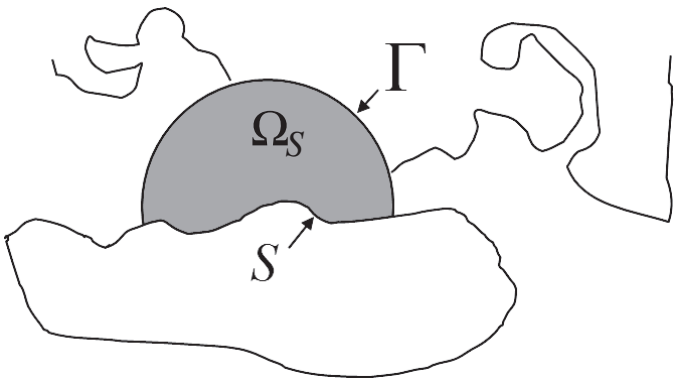

FIG. 4.1. *Illustration of the BIE-WOS method for finding Neumann data over a patch S on a curved boundary.*

solution $u(\mathbf{y})$ is needed. On the other hand, both the solution $u(\mathbf{y})$ and its normal derivative $\frac{\partial u(\mathbf{y})}{\partial \mathbf{n}}$ appear in the integral over S. As before, the solution $u(\mathbf{y})$ over Γ can be computed with the Feynman–Kac formula (2.9) using the WOS method. Then, the Neumann data over S can be solved from the following integral equation:

$$K\left[\frac{\partial u}{\partial \mathbf{n}}\right](\mathbf{x}) = b(\mathbf{x}), \quad \mathbf{x} \in S, \tag{4.2}$$

where

$$K\left[\frac{\partial u}{\partial \mathbf{n}}\right] \equiv \int_S G(\mathbf{x},\mathbf{y}) \frac{\partial u(\mathbf{y})}{\partial \mathbf{n_y}} ds_y, \tag{4.3}$$

and

$$b(\mathbf{x}) \equiv \left[\frac{u(\mathbf{x})}{2} + \text{p.v.} \int_S \frac{\partial G(\mathbf{x},\mathbf{y})}{\partial \mathbf{n_y}} u(\mathbf{y}) ds_y\right] + \int_\Gamma \frac{\partial G(\mathbf{x},\mathbf{y})}{\partial \mathbf{n_y}} u(\mathbf{y}) ds_y. \tag{4.4}$$

Here, p.v. stands for the Cauchy principal value of the double layer potential [25].

The integral equation of the first kind (4.2) is ill-conditioned and may cause numerical difficulties especially when the linear algebraic system arising from discretization is large. When that happens, a well-conditioned integral equation of the second kind can be obtained by taking normal derivatives of both sides of (4.1), resulting in the following identity:

$$\begin{aligned} \frac{\partial}{\partial \mathbf{n_x}} u(\mathbf{x}) = &- \int_\Gamma \frac{\partial^2 G(\mathbf{x},\mathbf{y})}{\partial \mathbf{n_x} \partial \mathbf{n_y}} u(\mathbf{y}) ds_y \\ &+ \int_S \left[-\frac{\partial^2 G(\mathbf{x},\mathbf{y})}{\partial \mathbf{n_x} \partial \mathbf{n_y}} u(\mathbf{y}) + \frac{\partial G(\mathbf{x},\mathbf{y})}{\partial \mathbf{n_x}} \frac{\partial u(\mathbf{y})}{\partial \mathbf{n_y}} \right] ds_y, \quad \mathbf{x} \in \Omega_S. \end{aligned} \tag{4.5}$$

If we let $\mathbf{x}$ approach the boundary S, we obtain the following second-kind integral equation:

$$\left(\frac{1}{2} I - D\right)\left[\frac{\partial u}{\partial \mathbf{n}}\right](\mathbf{x}) = b(\mathbf{x}), \quad \mathbf{x} \in S, \tag{4.6}$$

where the integral operator of the double layer potential is

$$D\left[\frac{\partial u}{\partial \mathbf{n}}\right](\mathbf{x}) \equiv \int_S \frac{\partial G(\mathbf{x},\mathbf{y})}{\partial \mathbf{n_x}} \frac{\partial u(\mathbf{y})}{\partial \mathbf{n_y}} ds_y, \tag{4.7}$$

and

$$b(\mathbf{x}) \equiv -\int_\Gamma \frac{\partial^2 G(\mathbf{x},\mathbf{y})}{\partial \mathbf{n_x} \partial \mathbf{n_y}} u(\mathbf{y}) ds_y - \text{p.f.} \int_S \frac{\partial^2 G(\mathbf{x},\mathbf{y})}{\partial \mathbf{n_x} \partial \mathbf{n_y}} u(\mathbf{y}) ds_y, \quad \mathbf{x} \in S. \tag{4.8}$$

Here, p.f. denotes the Hadamard finite part limit for the hyper-singular integral, which can be handled by a regularization technique [25].

BIE-WOS Algorithm. The BIE-WOS method for Neumann data over a patch S consists of the following two steps:

- Step 1. Apply the Feynman–Kac formula (2.9) using the WOS sampling technique to compute the solution $u(\mathbf{y}_{i,j})$ at Gauss quadrature points $\mathbf{y}_{i,j} \in \Gamma$, and compute the right-hand-side function $b(\mathbf{x})$ in (4.4) or (4.8) by appropriate Gauss quadratures.
- Step 2. Solve the BIE (4.2) or (4.6) with a collocation method to obtain the Neumann data $\frac{\partial u}{\partial \mathbf{n}}$ over S.

Remark. To find the derivatives of the potentials inside and outside a bounded domain Ω, the BIE-WOS method is applied separately, namely, to the hemisphere Ω_S in Figure 4.1 located in the interior and the exterior of Ω (wherein the WOS method is used), respectively. Once the Neumann data for the respective potential is found by the BIE-WOS method, the integral representation (2.3) can be used with the corresponding Green's function to obtain the potential in the whole interior or exterior space.

5. Numerical results. In this section, a series of numerical tests are presented to demonstrate the accuracy and efficiency of the proposed BIE-WOS method for finding Neumann data at a single point on a flat boundary or over a patch on a curved boundary.

5.1. Finding Neumann data at a single point on a flat boundary.

5.1.1. Regularization of hyper-singular integrals. First, let us present a regularization method using the simple solution of the Laplace equation [26] to compute the hyper-singular integral in (3.14) and (4.8). After some simple calculations, the term Σ_2 of (3.14) is found to be a Hadamard finite part limit of a hyper-singular integral, i.e.,

$$\Sigma_2 = -\lim_{\mathbf{x}'\to\mathbf{x}} \int_{S_a} \frac{\partial^2 g(\mathbf{x}',\mathbf{y})}{\partial \mathbf{n}_\mathbf{x} \partial \mathbf{n}_\mathbf{y}} u(\mathbf{y}) ds_y = -\text{p.f.} \int_{S_a} \frac{1}{2\pi} \left(\frac{1}{\rho^3} - \frac{1}{a^3} \right) u(\mathbf{y}) ds_y, \tag{5.1}$$

where $\rho = |\mathbf{x} - \mathbf{y}|$ for $\mathbf{x}$, $\mathbf{y} \in S_a$. The finite part (p.f.) limit of Hadamard type is defined by removing a divergent part in the process of defining a principal value (i.e., by removing a small patch of size ε centered at $\mathbf{x}$ and then letting ε approach zero) [25]. However, for the Laplace equation considered here, we can regularize this hyper-singularity by invoking an integral identity for the special constant solution $u \equiv \phi(\mathbf{x})$ with $\mathbf{x}$ being fixed. Namely, the integral identity (3.12) applied to this constant solution results in

$$0 = -\int_\Gamma \frac{\partial^2 g(\mathbf{x},\mathbf{y})}{\partial \mathbf{n}_\mathbf{x} \partial \mathbf{n}_\mathbf{y}} \phi(\mathbf{x}) ds_y - \lim_{\mathbf{x}'\to\mathbf{x}} \int_{S_a} \frac{\partial^2 g(\mathbf{x}',\mathbf{y})}{\partial \mathbf{n}_\mathbf{x} \partial \mathbf{n}_\mathbf{y}} \phi(\mathbf{x}) ds_y, \quad \mathbf{x} \in S. \tag{5.2}$$

Subtracting (5.2) from (3.15), we have a modified formula for the Neumann data:

$$\frac{\partial}{\partial \mathbf{n}_\mathbf{x}} u(\mathbf{x}) = \Sigma_1' + \Sigma_2', \qquad \mathbf{x} \in S, \tag{5.3}$$

where Σ_1' and Σ_2' are now the regularized versions of Σ_1 and Σ_2 in (3.13) and (3.14), respectively, i.e.,

$$\Sigma_1' = -\int_\Gamma \frac{\partial^2 g(\mathbf{x},\mathbf{y})}{\partial \mathbf{n}_\mathbf{x} \partial \mathbf{n}_\mathbf{y}} \left(u(\mathbf{y}) - \phi(\mathbf{x}) \right) ds_y, \tag{5.4}$$

and

$$\begin{aligned} \Sigma_2' &= -\lim_{\mathbf{x}'\to\mathbf{x}} \int_{S_a} \frac{\partial^2 g(\mathbf{x}',\mathbf{y})}{\partial \mathbf{n}_\mathbf{x} \partial \mathbf{n}_\mathbf{y}} \left(u(\mathbf{y}) - \phi(\mathbf{x}) \right) ds_y \\ &= -\lim_{\mathbf{x}'\to\mathbf{x}} \int_{S_a} \frac{1}{2\pi} \left(\frac{1}{r^3} - \frac{1}{a^3} \right) \left(\phi(\mathbf{y}) - \phi(\mathbf{x}) \right) ds_y, \end{aligned} \tag{5.5}$$

where $\mathbf{x}' = \mathbf{x} + (0,0,\varepsilon)$, $r = \sqrt{\rho^2 + \varepsilon^2}$, $\boldsymbol{\rho} = \mathbf{x} - \mathbf{y}$, and $\rho = |\mathbf{x} - \mathbf{y}|$ for $\mathbf{x}, \mathbf{y} \in S_a$. Moreover, the boundary condition $u(\mathbf{y}) = \phi(\mathbf{y})$ for $\mathbf{y} \in S_a$ has been invoked in (5.5).

Compared with (5.1), the singularity in the integral Σ_2' in (5.5) has been weakened by a factor of $\phi(\mathbf{y})-\phi(\mathbf{x})$, which vanishes at $\mathbf{y}=\mathbf{x}$. Therefore, Σ_2' can be evaluated by a regular Gauss quadrature. Let us consider only the integral involving the singular term $\frac{1}{r^3}$ in Σ_2', which is denoted by Σ_2^*, i.e.,

$$\Sigma_2^* = -\frac{1}{2\pi}\lim_{\mathbf{x}'\to\mathbf{x}}\int_{S_a}\frac{1}{r^3}\left(\phi(\mathbf{y})-\phi(\mathbf{x})\right)ds_y. \tag{5.6}$$

Consider a circular patch Λ_δ of radius δ centered at $\mathbf{x}$. Then Σ_2^* can be split further into two integrals as follows:

$$\begin{aligned}\Sigma_2^* &= -\frac{1}{2\pi}\int_{S_a\setminus\Lambda_\delta}\frac{1}{\rho^3}\left(\phi(\mathbf{y})-\phi(\mathbf{x})\right)ds_y\\ &\quad -\frac{1}{2\pi}\lim_{\mathbf{x}'\to\mathbf{x}}\int_{\Lambda_\delta}\frac{1}{r^3}\left(\phi(\mathbf{y})-\phi(\mathbf{x})\right)ds_y\\ &= -\frac{1}{2\pi}\int_{S_a\setminus\Lambda_\delta}\frac{1}{\rho^3}\left(\phi(\mathbf{y})-\phi(\mathbf{x})\right)ds_y+\Delta.\end{aligned} \tag{5.7}$$

To estimate the term Δ, we apply the following Taylor expansion of the boundary data $\phi(\mathbf{y})$ at $\mathbf{x}$:

$$\phi(\mathbf{y})-\phi(\mathbf{x}) = \nabla\phi(\mathbf{x})\cdot\boldsymbol{\rho}+O(\rho^2). \tag{5.8}$$

Then we have

$$\begin{aligned}\Delta &= -\frac{\nabla\phi(\mathbf{x})}{2\pi}\cdot\lim_{\mathbf{x}'\to\mathbf{x}}\int_{\Lambda_\delta}\frac{\boldsymbol{\rho}}{r^3}ds_y+\frac{1}{2\pi}\int_{\Lambda_\delta}\frac{O(\rho^2)}{r^3}ds_y\\ &= -\frac{\nabla\phi(\mathbf{x})}{2\pi}\cdot\lim_{\mathbf{x}'\to\mathbf{x}}\int_0^\delta\int_0^{2\pi}\frac{\rho(\cos\theta,\sin\theta)}{(\rho^2+\varepsilon^2)^{3/2}}\rho d\theta d\rho\\ &\quad+\lim_{\mathbf{x}'\to\mathbf{x}}\int_0^\delta\frac{O(\rho^2)}{(\rho^2+\varepsilon^2)^{3/2}}\rho d\rho\\ &= 0+\lim_{\mathbf{x}'\to\mathbf{x}}\int_0^\delta\frac{O(\rho^3)}{(\rho^2+\varepsilon^2)^{3/2}}d\rho.\end{aligned} \tag{5.9}$$

Now for all positive $\varepsilon>0$, we have

$$\frac{\rho^3}{(\rho^2+\varepsilon^2)^{3/2}}\le 1. \tag{5.10}$$

As a result, the following estimate of Δ holds uniformly for all positive ε:

$$\Delta = O(\delta). \tag{5.11}$$

Thus the regularized integral Σ_2^* can be approximated by the integral over $S_a\setminus\Lambda_\delta$ with an error of $O(\delta)$, i.e.,

$$\Sigma_2^* = -\frac{1}{2\pi}\int_{S_a\setminus\Lambda_\delta}\frac{1}{\rho^3}\left(\phi(\mathbf{y})-\phi(\mathbf{x})\right)ds_y+O(\delta). \tag{5.12}$$

5.1.2. Gauss quadratures over Γ and $S_a\setminus\Lambda_\delta$ and WOS. To compute the integral Σ_1' by a Gauss quadrature, we use $N_{g1}\times N_{g1}$ Gauss points over the hemi-

spherical surface Γ, and we have

$$\Sigma_1' \simeq -\sum_{i,j=1}^{N_{g1}} \omega_i \omega_j \frac{\pi^2}{4}(a^2 \sin\theta_i)\frac{3}{2a}\left(\frac{\cos\theta_i}{\pi a^2}\right)\left(u(\mathbf{y}_{i,j}) - \phi(\mathbf{x})\right), \tag{5.13}$$

where

$$\theta_i = \frac{\pi}{4}(\xi_i + 1), \varphi_j = \pi(\xi_j + 1), \mathbf{y}_{i,j} = (a, \theta_i, \varphi_j), \tag{5.14}$$

and ω_i and $\xi_i, 1 \le i \le N_{g1}$, are the weights and the locations of the Gauss points of the quadrature, respectively. Note that the term $\frac{\pi^2}{4}(a^2 \sin\theta_i)$ in (5.13) is the area of the surface element in spherical coordinates.

Now, for each point $\mathbf{y}_{i,j} \in \Gamma$, the value of the solution u at the point, namely, $u(\mathbf{y}_{i,j})$, is obtained by the Feynman–Kac formula (2.9) with N_{path} Brownian particles all starting from $\mathbf{y}_{i,j}$, namely,

$$u(\mathbf{y}_{i,j}) \simeq \frac{1}{N_{\text{path}}} \sum_{\text{k}=1}^{N_{\text{path}}} \phi(\mathbf{e}_k), \tag{5.15}$$

where $\mathbf{e}_k$ is the location on the domain boundary $\partial\Omega$ where the kth path terminates.

Note that the total number of Brownian particles needed in the BIE-WOS method is thus

$$N_{\text{path}-\text{bie}-\text{wos}} = N_{g1} \times N_{g1} \times N_{\text{path}}. \tag{5.16}$$

Finally, Σ_2^* in (5.12) can be computed by using another quadrature with $N_{g2} \times N_{g2}$ Gauss points to evaluate the integral over the ring-shaped region $S_a \backslash \Lambda_\delta$.

5.1.3. Numerical tests. In this subsection, we present several numerical tests to demonstrate the accuracy and efficiency of the proposed BIE-WOS method for finding Neumann data at a given point on a flat boundary for general Dirichlet boundary data. For comparison, we also implement the last-passage Monte Carlo method proposed in [13]. For comparison of accuracy, the charge density is calculated with FastCap, an open-source code developed at MIT [3] for 3-D capacitance extraction. FastCap is an indirect BEM, accelerated by the FMM, and the related linear system is solved by a conjugate gradient method. For the case of complex potentials on surfaces, we additionally implement a direct BEM (DBEM) [5]. In order to identify Brownian particles that have gone to infinity, in our tests a large sphere of radius of 10^5 is used. A sphere of this size is found to be large enough for desired accuracy, namely, once a particle moves out of this large sphere, it is considered as having gone to infinity.

• *Test* 1. *Charge densities on a planar interface between two dielectric half spaces.*

As shown in Figure 5.1, the whole space is divided by the plane $z = 0$ into two dielectric domains, and the dielectric constants for the upper and the lower domains are ϵ_0 and ϵ_1, respectively. A charge q is located in the lower domain at $\mathbf{r}_s = (0, 0, -h)$. Then the potential in the upper half space is given by

$$u(\mathbf{r}) = \frac{q'}{4\pi\epsilon_0}\frac{1}{|\mathbf{r} - \mathbf{r}_s|}, \quad q' = \frac{2\epsilon_0}{\epsilon_0 + \epsilon_1} q. \tag{5.17}$$

Note that $u(\mathbf{r})$ satisfies the Laplace equation $\nabla^2 u(\mathbf{r}) = 0$ for $z > 0$ with variable Dirichlet data on the boundary $z = 0$.

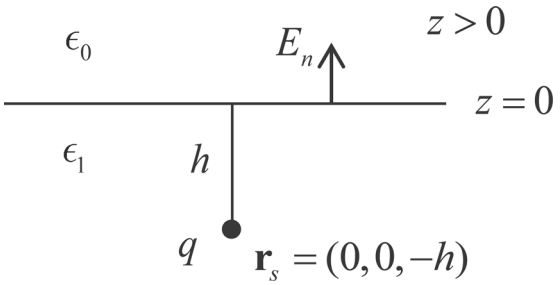

FIG. 5.1. *Two dielectric half spaces separated by the planar interface $z = 0$.*

TABLE 5.1
Charge density on the planar interface with different radii of the hemisphere.

	Last-passage		BIE-WOS				Analytical
a	Σ_{LP}	err%	Σ_1'	Σ_2'	$\Sigma_1' + \Sigma_2'$	err%	solution
0.1	0.698543	2.38	0.69884	0.018777	0.717612	0.29	
0.2	0.677996	5.25	0.67784	0.037515	0.715355	0.03	
0.5	0.622949	12.94	0.62146	0.093054	0.714517	0.14	0.71554
0.7	0.586721	18.00	0.58432	0.128971	0.713287	0.32	
1.0	0.534695	25.27	0.53659	0.179973	0.716562	0.14	

The numerical results for the charge density at the point $\mathbf{x} = (0.5, 0, 0)$ obtained by the last-passage method and the BIE-WOS method, with various values of the radius a of the hemisphere, are listed in Table 5.1. In the last-passage method, the total number of sampling paths is $N = 4 \times 10^5$. In the BIE-WOS method, the total number of Gauss points is $N_{g1} \times N_{g1} = 20 \times 20$ for the integral over the hemispherical surface Γ, and $N_{g2} \times N_{g2} = 20 \times 20$ for the integral over the 2-D disk S_a. Starting from each Gauss point on Γ, the number of sampling paths is $N_{\text{path}} = 10^3$. Therefore, the total number of sampling paths for the BIE-WOS method is also 4×10^5. The thickness ε of the absorption shell for the WOS technique is taken to be 10^{-5} in both methods.

From Table 5.1, we can see that as the radius a increases, the relative error of the last-passage method grows as high as 25.27%. It implies that when the Dirichlet data of the potential on the disk S_a is not constant, the last-passage method breaks down since the variable potential inside the disk S_a influences the charge density at $\mathbf{x}$. In contrast, the BIE-WOS method takes into account such influence as demonstrated by the numerical results, and most importantly, its accuracy is insensitive to the radius a and its maximal relative error is less than 0.32% for all a between 0.1 and 1.0.

Table 5.2 lists the accuracy of the desingularized Σ_2' in (5.12) with different values of δ and different numbers of Gauss points $N_{g2} \times N_{g2}$, where the location of the sought-after density is at $(0.5, 0, 0)$. The result with $N_{g2} \times N_{g2} = 20 \times 20$ and with $\delta/a = 10^{-6}$ is taken as the reference value for Σ_2'. Table 5.2 shows the convergence of Σ_2' as δ/a goes to zero and the number of Gauss points increases. Also, it can be seen that when the number of Gauss points becomes large enough, for example, 20×20, the relative error is on the order of δ/a, verifying the estimate in (5.12).

• *Test* 2. *Four rectangular plates with a piecewise constant potential distribution.*

A 3-D structure with four rectangular plates is depicted in Figure 5.2, where the length, the width, and the thickness of all four plates are 1m, 1m, and 0.01m, respectively. We first set the potential of the plate II to 1V and the potentials of the other three plates to 0V, and then we compute the charge density at the point

TABLE 5.2
Accuracy of the desingularization in (5.12).

δ/a	Σ_2' calculated by Gauss quadrature with $N_{g2} \times N_{g2}$ points							
	4×4	err%	6×6	err%	10×10	err%	20×20	err%
10^{-1}	0.09659	3.800	0.08983	3.462	0.08949	3.833	0.08949	3.8351
10^{-2}	0.10042	7.916	0.09306	0.001	0.09273	0.347	0.09273	0.3492
10^{-3}	0.10083	8.352	0.09335	0.314	0.09302	0.033	0.09302	0.0346
10^{-4}	0.10087	8.397	0.09337	0.345	0.09305	0.002	0.09305	0.0035
10^{-5}	0.10087	8.402	0.09338	0.348	0.09306	0.001	0.09305	0.0003
10^{-6}	0.10087	8.402	0.09338	0.348	0.09306	0.001	0.09305	

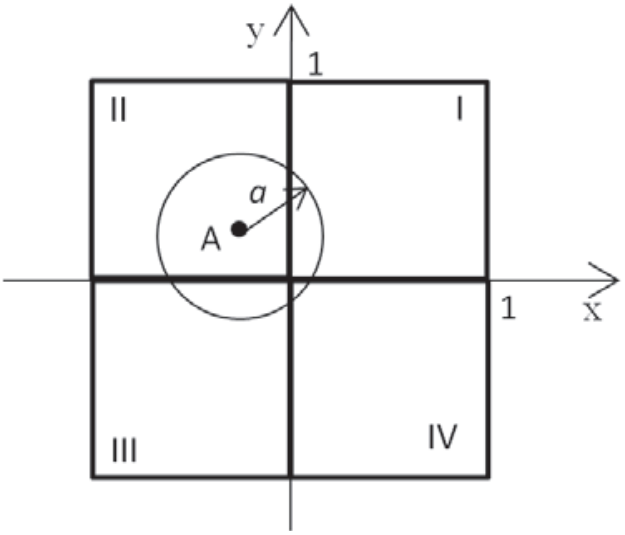

FIG. 5.2. *Four plates at different potentials.*

$A(-0.2273, 0.2273, 0)$. The numerical results of all four methods are listed in Table 5.3, where the result obtained by FastCap with each side of the plates being discretized into 99×99 panels is taken to be the reference solution. The DBEM uses the discretization with 11×11 panels on each side, and its relative error is 0.46%.

Both the last-passage and the BIE-WOS methods are tested with various values of the radius a of the hemisphere, and the other parameters are the same as used in Test 1. In this case, the integral Σ_2' is related to the area of the intersection between the disk S_a and the plates I, III, and IV, and we compute it directly by the *quad* function in MATLAB, instead of by Gauss quadrature.

Note that the potential on the domain boundary $\partial\Omega$ is piecewise constant. Therefore, in the last-passage method, the charge density should be computed, instead of by (3.10), by the following formula:

$$\Sigma_{\mathrm{LP}} = \frac{3}{2a} \frac{N_{\mathrm{inf}} + N_I + N_{III} + N_{IV}}{N_{\mathrm{path-LP}}}, \tag{5.18}$$

where $N_{\mathrm{inf}}, N_I, N_{III}$, and N_{IV} represent the total number of particles that have gone to infinity, to the plate I, to the plate III, and to the plate IV, respectively, and

TABLE 5.3
Charge density of a structure of four unit plates with different radii of the hemisphere.

a	Last-passage		BIE-WOS				DBEM	
	$\Sigma_{\rm LP}$	err%	Σ_1'	Σ_2'	$\Sigma_1'+\Sigma_2'$	err%	value	err%
0.1	2.6084	0.05	2.6051	0	2.6051	0.07	2.595	0.46
0.2	2.6026	0.17	2.6051	0	2.6051	0.07		
0.2273	2.6099	0.11	2.6064	0	2.6064	0.02		
0.3	2.5252	3.14	2.5178	0.0892	2.6070	0.00	Fastcap	
0.5	1.9698	24.44	1.9692	0.6330	2.6022	0.19	2.607	
0.7	1.5779	39.48	1.5784	1.0271	2.6055	0.06		

TABLE 5.4
Charge density of a structure of four unit plates with complex potentials.

a	Last-passage		BIE-WOS				DBEM
	$\Sigma_{\rm LP}$	err%	Σ_1'	Σ_2'	$\Sigma_1'+\Sigma_2'$	err%	value
0.1	−0.4522	3.92	−0.4454	−0.008617	−0.4540	3.54	−0.4707
0.2	−0.4442	5.62	−0.4444	−0.01722	−0.4616	1.93	
0.3	−0.4369	7.17	−0.4362	−0.02579	−0.4620	1.85	
0.4	−0.4288	8.90	−0.4278	−0.03433	−0.4621	1.82	
0.5	−0.4203	10.7	−0.4202	−0.04280	−0.4630	1.62	

$N_{\rm path-LP}$ denotes the total number of Brownian paths starting from the hemispherical surface Γ.

From Table 5.3, we can see that when $a \le 0.2273$, i.e., when the disk S_a is totally contained in the plate II, the last-passage method works with a maximal relative error less than 0.17%. However, once S_a becomes large and touches plates with different potentials, the relative error of the last-passage method increases to be even as high as 39.48%. In comparison, the accuracy of the BIE-WOS method is insensitive to the radius a, with a maximal relative error less than 0.19% for radius a between 0.1 and 0.7. This again confirms the fact that the last-passage method of [13] is designed for conducting surfaces only (i.e., constant potentials), but not for surfaces of variable potentials. Therefore, it should not be used when the disk S_a includes regions of different potentials.

In conclusion, for a general variable potential, the last-passage method is limited while the BIE-WOS method is free of the constraint of constant boundary potentials.

• *Test* 3. *Four rectangular plates with a complex potential distribution.*

To further emphasize the point raised above in Test 2, we now consider the four plates with the complex potential distribution

$$\phi(x,y) = \sin mx \sin ny. \tag{5.19}$$

As we will see, to obtain an accurate result, the last-passage method requires increasingly smaller radius a for larger m and n to achieve an (approximately) constant potential within the disk S_a.

The numerical results of the charge density at the point $(-0.5, 0.5, 0)$ obtained by the last-passage method, the BIE-WOS method, and the DBEM are shown in Table 5.4. We take the result of the DBEM with 17×17 panels on each plate as the reference solution. All other parameters in the BIE-WOS and the last-passage methods are the same as in the previous case. From Table 5.4, we can see that the BIE-WOS method has better accuracy.

The relative error versus the number of Gauss points and the number of WOS paths are shown in Figure 5.3. The BIE-WOS result with $N_{g1} \times N_{g1} = 20 \times 20$,

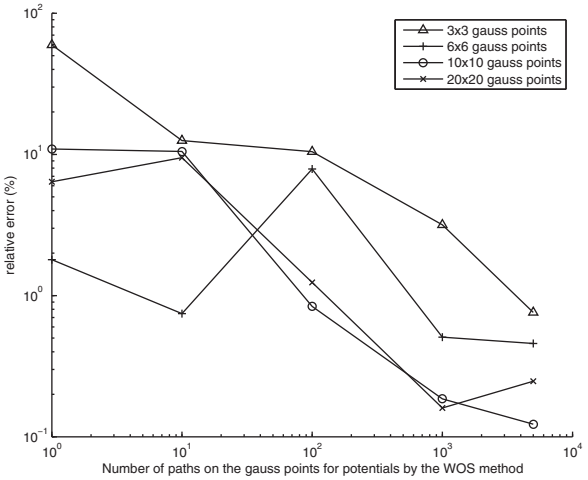

FIG. 5.3. *Convergence of the BIE-WOS method vs. the number of Brownian paths and the number of Gauss points.*

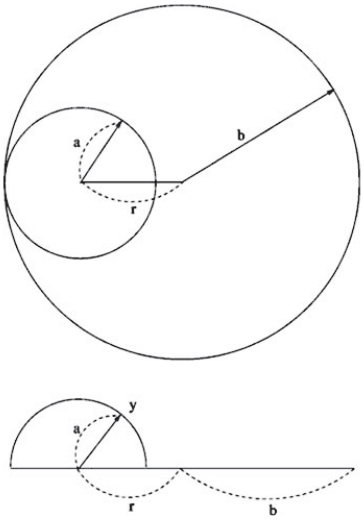

FIG. 5.4. *Finding the charge distribution over a disk in the* 3*-D space.*

$N_{g2}\times N_{g2} = 10\times 10$, $N_{\text{path}} = 2\times 10^3$, and $a = 0.5$ is taken as the reference solution. From Figure 5.3, we can see that when the total number of Brownian paths N_{path} is larger than 10^3 at each Gauss point, the BIE-WOS result with 10×10 Gauss points achieves an accuracy of about 1% in relative error.

• *Test* 4. *CPU time comparison.*

For both the last-passage and the BIE-WOS methods, the CPU time is expected to be linear in terms of the total number of random paths. We demonstrate this fact with the case of a thin circular disk of radius b in the 3-D space [13] as shown in Figure 5.4. From [27], the analytical result for the charge density on the disk is

$$\sigma(\rho) = \frac{Q}{4\pi b\sqrt{b^2-\rho^2}}, \quad Q = 8b. \tag{5.20}$$

TABLE 5.5
The relative error and the CPU time vs. the number of random paths.

Last-passage				BIE-WOS			
$N_{\text{path}-\text{LP}}$	Σ_{LP}	err%	CPU time(s)	$N_{\text{path}-\text{bie}-\text{wos}}$	$\Sigma_1' + \Sigma_2'$	err%	CPU time(s)
10^4	0.69975	4.81	32	$10^2 \cdot 100 = 10^4$	0.68888	6.29	30
10^5	0.73253	0.35	331	$10^2 \cdot 1000 = 10^5$	0.73960	0.61	307
$4 \cdot 10^5$	0.73743	0.32	1325	$20^2 \cdot 1000 = 4 \cdot 10^5$	0.73441	0.09	1218

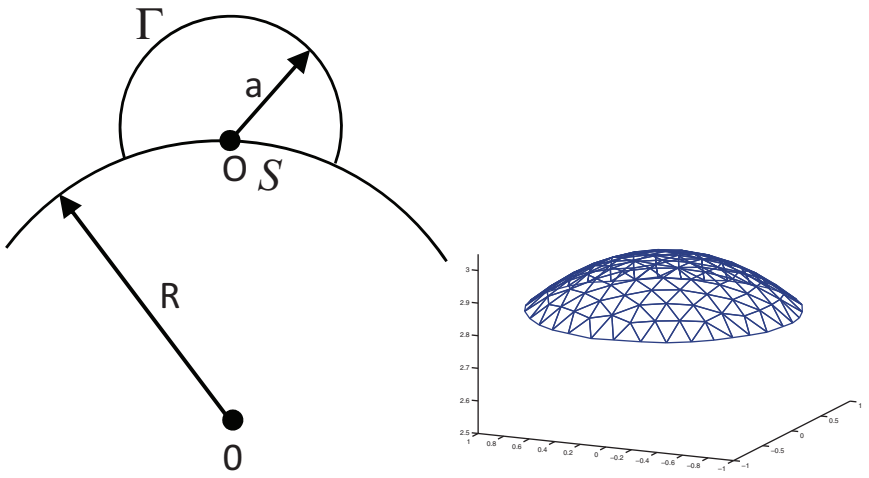

FIG. 5.5. *Left: BIE-WOS setting for finding the Neumann data over a patch on the surface of a large sphere. Right: the triangular mesh over the patch.*

For a given tolerance on the relative error of the charge density at $(-0.5, 0, 0)$, the CPU time versus the number of random paths are listed in Table 5.5. The radius of the disk S_a is taken to be $a = 0.4$ and that of the thin disk is taken to be $b = 1$, respectively. The analytical charge density at $(-0.5, 0, 0)$ is $\sigma(0.5) = 0.735105$. From Table 5.5, we can see that the CPU time for both methods is indeed in proportion to the total number of random paths for a given accuracy. Although in this case the integral Σ_2' in the BIE-WOS method is obviously zero, we still evaluate it as if for a general variable boundary potential and the CPU time for calculating Σ_2' is included in the total CPU time of the BIE-WOS method displayed in Table 5.5. It is noted that the CPU time in computing the integral Σ_2' for all cases is insignificant and is, for example, only about 0.012 second for a 20×20 Gauss quadrature.

5.2. Finding Neumann data over a patch of a curved boundary. Next, to test the BIE-WOS method for curved boundaries, we compute the DtN mapping on a large sphere as shown in Figure 5.5 (left) with radius $R = 3$. A point charge $q = 1$ is located at the center O of the sphere. The analytical result for the potential is then known. To compute the Neumann data over a local patch S around the point $\mathbf{o} = (0, 0, 3)$ on the surface of the large sphere, a small sphere with radius $a = 1$ is superimposed over the point $\mathbf{o}$. The local patch S is discretized with a triangular mesh as shown in Figure 5.5 (right).

The BIE (4.2) is solved using a collocation BEM. When a collocation point is not inside an integration panel, a simple Gauss quadrature is used. For collocation points

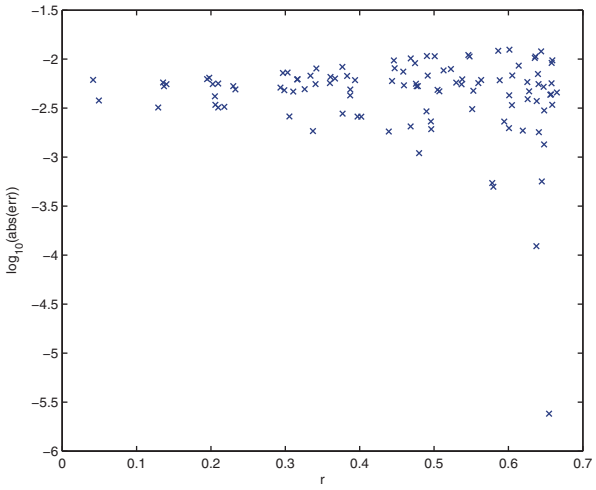

FIG. 5.6. *Accuracy of the Neumann data obtained by the BIE-WOS method over the patch S.*

inside an integration panel, both weak and strong singularities occur; however, they can be regularized by a local polar transformation and a direct evaluation method [28], respectively. In particular, in this test, a Gauss quadrature using 20×20 points is employed in the panel. For the integrals on Γ, a Gauss quadrature using 30×30 points is used. The potential $u(\mathbf{y})$ on Γ is computed by the Feynman–Kac formula and the WOS method with 10^4 Brownian paths on a regular grid generated by evenly discretizing the surface of the small sphere along the polar and azimuthal angles. The values of $u(\mathbf{y})$ on Γ but not on the grid points, as required by numerical quadratures, are obtained by interpolating its values on the grid points.

The relative errors of the Neumann data at the centers of the triangular panels on S are shown in Figure 5.6, where the x-axis represents the distance r between the center of a triangle and the point $\mathbf{o}$. From Figure 5.6, we can see that for the panels close to the point $\mathbf{o}$, i.e., for the panels with $r < 0.7a$, the maximal relative error is less than 1.25%, which is accurate enough for most engineering applications. It is noted that due to the sharp corner-edge singularity of the domain Ω_S where the hemisphere and the domain boundary $\partial\Omega$ intersect, the piecewise constant collocation BEM method loses some of its accuracy, which limits the region of acceptable accuracy of the BEM solution for the sought-after Neumann data. This well-known problem in singular boundary elements usually is addressed with graded meshes near the edge singularity [29], [30], [31] and is still an active research topic in BEMs [32]. A resolution of this edge singularity can increase the size of the region of useful BEM solutions in the BIE-WOS algorithm and can be incorporated into the algorithm. As to be discussed in section 6, the domain boundary $\partial\Omega$ will be covered with overlapping patches S_i, so the loss of the accuracy of the BEM solution near the edge of each patch will not hinder the use of the BIE-WOS method. However, any improvement of the BEM near the edge will reduce the total number of patches needed to cover the boundary, thus reducing the total computational cost.

6. Conclusions and discussions. In this paper we have proposed a local BIE-WOS method that combines a local deterministic singular BIE method and the Monte Carlo WOS algorithm to find Neumann data on general boundaries with given Dirichlet data. The singular integral equation method for the Neumann data over a local

patch on the boundary surface involves the solution of the potential on a local hemisphere, which can be readily obtained with the Feynman–Kac formula with the help of the WOS sampling technique of Brownian paths. Numerical results have validated the accuracy and efficiency of the BIE-WOS method.

The local BIE-WOS method of finding the DtN or NtD mapping can produce a parallel algorithm for the solution of a Poisson equation with Dirichlet or Neumann boundary conditions. First, the whole domain boundary $\partial\Omega$ is partitioned into a union of overlapping patches S_i, namely,

$$\partial\Omega = \cup_i S_i.$$

Then, the local BIE-WOS method can be used to find the DtN or NtD mapping over each patch S_i independently and in parallel. In principle, the computation of the BIE-WOS method over each patch can be done on one processor without need for communication with other processors; thus a high parallel scalability can be expected. Second, the solution of the Laplace equation in the whole space can be found using the integral representation (2.3) with the help of *one application* of FMM [12].

Several important issues, however, have to be addressed before the BIE-WOS method can be used for large-scale computation of Poisson or modified Helmholtz equations. The first issue is how to deal with NtD mapping problems where Neumann data are given on the boundary and Dirichlet data are required. In this case, the Feynman–Kac formula derived in [33] can be used, which involves reflecting Brownian paths [34] with respect to the domain boundary. Efficient numerical implementation of the formula will have to be developed. The second issue is how to handle the modified Helmholtz equation. Even though a corresponding Feynman–Kac formula is available [33], a survival factor will be introduced as the WOS method samples the Brownian paths, and efficient ways to use the Feynman–Kac formula will have to be developed. The third issue is that, since the WOS scheme requires the distance between a Brownian particle and the domain boundary, efficient algorithms for the computation of such distance will also have to be developed for the overall efficiency of the BIE-WOS method.

The parallel algorithm based on the BIE-WOS method for solving Poisson or modified Helmholtz equations has the following important features:

- It is noniterative in construction and does not need to solve any global linear system.
- It is stochastic in nature based on the fundamental link between Brownian motion and solutions of elliptic PDEs.
- It has massive parallelism that is suitable for the large number of processors needed for large-scale computing due to the random walk and local integral equation components of the algorithm.
- It does not need traditional finite-element type surface or volume meshes.
- It is applicable to complex 3-D geometries with accurate treatment of domain boundaries.

In comparison with traditional finite element and finite difference methods, the BIE-WOS solver is suitable for only Poisson and modified Helmholtz equations (due to the use of WOS-type sampling techniques of the diffusion paths), and its accuracy is limited to that of the Monte Carlo sampling technique, while the traditional grid-based methods can handle more general PDEs with variable coefficients and achieve high accuracy. Nonetheless, since solutions of the Poisson and modified Helmholtz equations form the bulk computations of projection-type methods for incompressible flows and other important scientific computing applications, the progress in scala-

bility of parallel BIE-WOS-based solvers will have a large impact on the simulation capability in these and other engineering applications.

Acknowledgments. The authors acknowledge the constructive suggestions of the reviewers and Drs. Shaozhong Deng and Joel Avrin regarding the presentation and organization of the materials, which have improved the paper.

REFERENCES

[1] A. J. Chorin, *Numerical solution of the Navier-Stokes equations*, Math. Comp, 22 (1968), pp. 745–762.
[2] R. Temam, *Navier-Stokes Equations: Theory and Numerical Analysis*, North-Holland, Amsterdam, 1984.
[3] K. Nabors and J. White, *Fastcap: A multipole accelerated 3-D capacitance extraction program*, IEEE Trans. Comput.-Aided Design Integr. Circuits Syst., 10 (1991), pp. 1447–1459.
[4] J. R. Phillips and J. White, *A precorrected-FFT method for capacitance extraction of complicated 3-D structures*, in Proceedings of the 1994 IEEE/ACM International Conference on Computer-Aided Design, IEEE Computer Society Press, 1994, pp. 268–271.
[5] W. Yu and Z. Wang, *Enhanced QMM-BEM solver for three-dimensional multiple-dielectric capacitance extraction within the finite domain*, IEEE Trans. Microw. Theory Techn., 52 (2004), pp. 560–566.
[6] W. Shi, J. Liu, N. Kakani, and T. Yu, *A fast hierarchical algorithm for three-dimensional capacitance extraction*, IEEE Trans. Comput.-Aided Design Integr. Circuits Syst., 21 (2002), pp. 330–336.
[7] S. Yan, V. Sarin, and W. Shi, *Sparse transformations and preconditioners for 3-D capacitance extraction*, IEEE Trans. Comput.-Aided Design Integr. Circuits Syst., 24 (2005), pp. 1420–1426.
[8] G. Chen, H. Zhu, T. Cui, Z. Chen, X. Zeng, and W. Cai, *ParAFEMCap: A parallel adaptive finite-element method for 3-D VLSI interconnect capacitance extraction*, IEEE Trans. Microw. Theory Techn., 60 (2012), pp. 218–231.
[9] C. A. Brebbia, *The Boundary Element Method in Engineering*, Pentech Press, London, 1978.
[10] A. Brandt, *Guide to multigrid development*, in Multigrid Methods, Springer, Berlin, 1982, pp. 220–312.
[11] A. Toselli and O. Widlund, *Domain decomposition methods-algorithms and theory*, Springer Ser. Comput. Math., Springer, Berlin, 2005.
[12] L. Greengard and V. Rokhlin, *A fast algorithm for particle simulations*, J. Comput. Phys., 73 (1987), pp. 325–348.
[13] J. A. Given, C. O. Hwang, and M. Mascagni, *First-and last-passage Monte Carlo algorithms for the charge density distribution on a conducting surface*, Phys. Rev. E, 66 (2002), 056704.
[14] K. K. Sabelfeld, *Monte Carlo methods in boundary value problems*, Springer Ser. Comput. Phys., Springer, Berlin, 1991.
[15] C. O. Hwang and J. A. Given, *Last-passage Monte Carlo algorithm for mutual capacitance*, Phys. Rev. E, 74 (2006), pp. 027701-1–3.
[16] Y. L. Le Coz and R. B. Iverson, *A stochastic algorithm for high speed capacitance extraction in integrated circuits*, Solid-State Electron., 35 (1992), pp. 1005–1012.
[17] Y. L. Le Coz, H. J. Greub, and R. B. Iverson, *Performance of random-walk capacitance extractors for IC interconnects: A numerical study*, Solid-State Electron., 42 (1998), pp. 581–588.
[18] M. I. Freidlin, *Functional Integration and Partial Differential Equations*, Princeton University Press, Princeton, NJ, 1985.
[19] A. Friedman, *Stochastic Differential Equations and Applications*, Dover Publications, New York, 2006.
[20] K. L. Chung, *Green, Brown and Probability*, World Scientific, Singapore, 1995.
[21] M. Mascagni and C. O. Hwang, *ϵ-shell error analysis for "walk on spheres" algorithms*, Math. Comput. Simulation, 63 (2003), pp. 93–104.
[22] M. E. Muller, *Some continuous Monte Carlo methods for the Dirichlet problem*, Ann. Math. Statist., 27 (1956), pp. 569–589.
[23] M. Mascagni and N. A. Simonov, *The random walk on the boundary method for calculating capacitance*, J. Comput. Phys., 195 (2004), pp. 465–473.

[24] K. K. Sabelfeld, I. A. Shalimova, and A. Lavrentjeva, *Random walk on spheres process for exterior Dirichlet problem*, Monte Carlo Methods Appl., 1 (1995), pp. 325–331.
[25] W. Cai, *Computational Methods for Electromagnetic Phenomena: Electrostatics in Solvation, Scattering, and Electron Transport*, Cambridge University Press, London, 2013.
[26] J. Giroire and J. C. Nedelec, *Numerical solution of an exterior Neumann problem using a double layer potential*, Math. Comp, 32 (1978), pp. 973–990.
[27] J. A. Given and C. O. Hwang, *Edge distribution method for solving elliptic boundary value problems with boundary singularities*, Phys. Rev. E, 68 (2003), pp. 046128-1–6.
[28] M. Guiggiani and A. Gigante, *A general algorithm for multidimensional Cauchy principal value integrals in the boundary element method*, J. Appl. Mech., 57 (1990), pp. 906–915.
[29] G. A. Chandler, *Galerkin's method for boundary integral equations on polygonal domains*, J. Aust. Math. Soc. Ser. B. Appl. Math., 26 (1984), pp. 1–13.
[30] K. Atkinson and I. Graham, *Iterative variants of the Nyström method for second kind boundary integral operators*, SIAM J. Sci. Stat. Comput., 13 (1990), pp. 694–722.
[31] R. Kress, *A Nyström method for boundary integral equations in domains with corners*, Numer. Math., 58 (1990), pp. 145–161.
[32] J. Bremer and V. Rokhlin, *Efficient discretization of Laplace boundary integral equations on polygonal domain*, J. Comput. Phys., 229 (2010), pp. 2507–2525.
[33] P. Hsu, *Probabilistic approach to the Neumann problem*, Comm. Pure Appl. Math., 38 (1985), pp. 445–472.
[34] P. L. Lions and A. S. Sznitman, *Stochastic differential equations with reflecting boundary conditions*, Comm. Pure Appl. Math., 37 (1984), pp. 511–537.